Direct measurement of the 3-dimensional DNA lesion distribution induced by energetic charged particles in a mouse model tissue

Johanna Mirsch[a], Francesco Tommasino[b], Antonia Frohns[a], Sandro Conrad[a], Marco Durante[b,c], Michael Scholz[b], Thomas Friedrich[b,1], and Markus Löbrich[a,1]

[a]Radiation Biology and DNA Repair, Darmstadt University of Technology, 64287 Darmstadt, Germany; [b]Department of Biophysics, GSI Helmholtz Center for Heavy Ion Research, 64291 Darmstadt, Germany; and [c]Institute for Condensed Matter Physics, Darmstadt University of Technology, 64289 Darmstadt, Germany

Edited by Rodney Rothstein, Columbia University Medical Center, New York, NY, and approved August 24, 2015 (received for review May 12, 2015)

Charged particles are increasingly used in cancer radiotherapy and contribute significantly to the natural radiation risk. The difference in the biological effects of high-energy charged particles compared with X-rays or γ-rays is determined largely by the spatial distribution of their energy deposition events. Part of the energy is deposited in a densely ionizing manner in the inner part of the track, with the remainder spread out more sparsely over the outer track region. Our knowledge about the dose distribution is derived solely from modeling approaches and physical measurements in inorganic material. Here we exploited the exceptional sensitivity of γH2AX foci technology and quantified the spatial distribution of DNA lesions induced by charged particles in a mouse model tissue. We observed that charged particles damage tissue nonhomogenously, with single cells receiving high doses and many other cells exposed to isolated damage resulting from high-energy secondary electrons. Using calibration experiments, we transformed the 3D lesion distribution into a dose distribution and compared it with predictions from modeling approaches. We obtained a radial dose distribution with sub-micrometer resolution that decreased with increasing distance to the particle path following a $1/r^2$ dependency. The analysis further revealed the existence of a background dose at larger distances from the particle path arising from overlapping dose deposition events from independent particles. Our study provides, to our knowledge, the first quantification of the spatial dose distribution of charged particles in biologically relevant material, and will serve as a benchmark for biophysical models that predict the biological effects of these particles.

charged particles | radial dose distribution | biodosimetry | γH2AX foci | local effect model

Charged particles, including protons, α-particles, and heavy ions, are increasingly used in cancer radiotherapy and represent a significant component of the natural background irradiation on earth and in space (1–3). Their biological effect is often very different from that of photons (X- or γ-rays), largely because charged particles deposit their energy along a track, whereas photons produce a fairly homogeneous dose distribution. Linear energy transfer (LET; typically given in units of keV/μm) has been introduced as a parameter to describe the amount of energy that charged particles deposit along their track. Particles with high LET are densely ionizing and typically biologically more effective than photons or low-LET particles.

Energy deposition along a particle track is not restricted to the path itself (the so-called "track core"), but extends laterally into an area known as the penumbra of the particle, which can reach considerable distances for high-energy particles. Energy deposition in the penumbra arises from energetic secondary electrons, so-called δ-electrons, which are generated by ionization events of the charged particles and carry energy away from the immediate path into the penumbra. According to classical track structure theory, ~50% of the total energy is deposited in the penumbra, where it spreads out over a much greater volume than the energy in the track core (4). Thus, the penumbra represents a sparsely ionized region within the track of high-LET particles. Thus, charged particles deposit their energy in a complex 3D manner and typically comprise a spectrum of high- and low-ionization densities. The total biological effect of a charged particle is a result of this complex energy deposition pattern.

Our knowledge about the energy deposition pattern of charged particles is based largely on theoretical predictions and physical measurements in inorganic material. Most information in this respect was gained from microdosimetric experiments with gas-filled detectors (5). In these devices, the dose distribution around an ion trajectory is measured and rescaled to a track structure profile in water by comparing the electron density of the gas with that of water. Such a density scaling approach is expected to fail, however, when the energies of the δ-electrons are in the same order of magnitude as the intermolecular binding energies (6, 7). These limitations call for alternative approaches for assessing the 3D energy deposition pattern of charged particles directly in biologically relevant material.

Computational models, mostly Monte Carlo codes, have been developed to describe the energy deposition patterns of charged particles. Results from such approaches are in reasonable agreement with physical measurements, although track structure modeling at a nanometer or micrometer scale remains a challenge.

Significance

Charged particles are applied in cancer radiotherapy because they are more efficient than X-rays or γ-rays in tumor cell killing. This efficiency results from the high dose deposition along the path of the particles. However, charged particles damage tissue inhomogeneously, such that many cells not directly hit by the particles receive a low dose and can survive with mutations. Because mutations can lead to secondary malignancies, this effect limits the applicability of charged particles in cancer radiotherapy. We provide the first direct measurement of the 3D DNA lesion distribution induced by energetic charged particles in a mouse model tissue. Our detailed analysis of the dose distribution will serve to benchmark biophysical models currently used for irradiation planning in cancer radiotherapy.

Author contributions: M.L. designed research; J.M., F.T., and A.F. performed research; J.M., F.T., A.F., S.C., M.D., M.S., T.F., and M.L. analyzed data; and J.M., T.F., and M.L. wrote the paper.

The authors declare no conflict of interest.

This article is a PNAS Direct Submission.

Freely available online through the PNAS open access option.

[1]To whom correspondence may be addressed. Email: t.friedrich@gsi.de or lobrich@bio.tu-darmstadt.de.

This article contains supporting information online at www.pnas.org/lookup/suppl/doi:10.1073/pnas.1508702112/-/DCSupplemental.

Computational models are also used to predict the biological effects of charged particles, such as the induction of DNA damage (8–11). Unlike Monte Carlo calculations, amorphous track structure models exploit the radial dose distribution to predict the biological response (12, 13). One of these approaches, known as the local effect model (LEM), is currently applied in particle cancer therapy to predict the biological effects of heavy ions (14, 15). The LEM assumes that the same local dose, independent of the radiation type that deposits this dose, leads to the same biological effect. Essentially, LEM derives the biological effects of charged particles from the response of cells or tissues to photon radiation.

Double-strand breaks (DSBs) are among the most hazardous DNA lesions induced by ionizing radiation (IR) because they can give rise to more complex lesions when occurring in clusters or associated with other lesions (16). On DSB induction, the histone variant H2AX is phosphorylated at the break site to γH2AX (17). This histone modification can be visualized by microscopy and forms so-called γH2AX foci, which arise within minutes after IR in a 1:1 ratio to isolated DSBs and are lost with time due to DSB repair (18, 19). Because this technology detects single isolated DSBs in single cells, it has exceptional sensitivity and can monitor the effect of IR doses of a few mGy (20, 21). Not surprisingly, γH2AX foci analysis has been applied to assess radiation doses encountered by humans during diagnostic medical procedures, such as computed tomography scanning (22–25). Moreover, this technology can be applied to different tissues (26, 27) and is becoming the gold standard for various biodosimetric applications (28, 29).

In the present study, we combined the particular sensitivity of the γH2AX foci technology with its second major advantage, the ability to precisely determine the position of the DNA lesions, to investigate the spatial distribution of γH2AX foci induced by charged particles. Calibration experiments allowed transformation of the lesion distribution into a 3D dose distribution, which could be compared with predictions from the amorphous track structure model, the LEM. Using this procedure, we were able to quantify the lateral (radial) dose profile of titanium (Ti) ions with submicrometer resolution and verify the theoretically predicted $1/r^2$ dose decline using a biological model system.

Results

Charged particles deposit high doses in the core (i.e., the inner part) of their track and low doses in the surrounding penumbra (i.e., the outer part). Because the physical dose deposited by δ-electrons in the outer part of the track is predicted to decrease strongly with the distance to the particle path (5, 30), we aimed to biologically quantify the dose in a 3D geometry around the path. We used mouse tissue as a model system and quantified DSBs by counting γH2AX foci, which arise linearly with radiation dose (18, 19, 31). To further enhance the sensitivity of this biodosimetric approach, we investigated the mouse retina with its densely packed and uniformly arranged photoreceptors (32). Lamin B staining showed that mouse photoreceptors contained a low amount of cytoplasm and little intercellular space (Fig. 1*A*). The nuclei of photoreceptors contained a central heterochromatic chromocenter, which is surrounded by euchromatic DNA (33) (Fig. 1*B*). This specialized chromatin structure represents a unique adaptation of photoreceptors to optimal vision in low-light conditions (33). Collectively, the various special features of the mouse retina make it an ideal model system for analyzing the spatial dose distribution of charged particles.

γH2AX Foci in Mouse Photoreceptors After Low X-Ray Doses. To characterize the formation of γH2AX foci in mouse photoreceptors, we quantified the number of foci per cell at different time

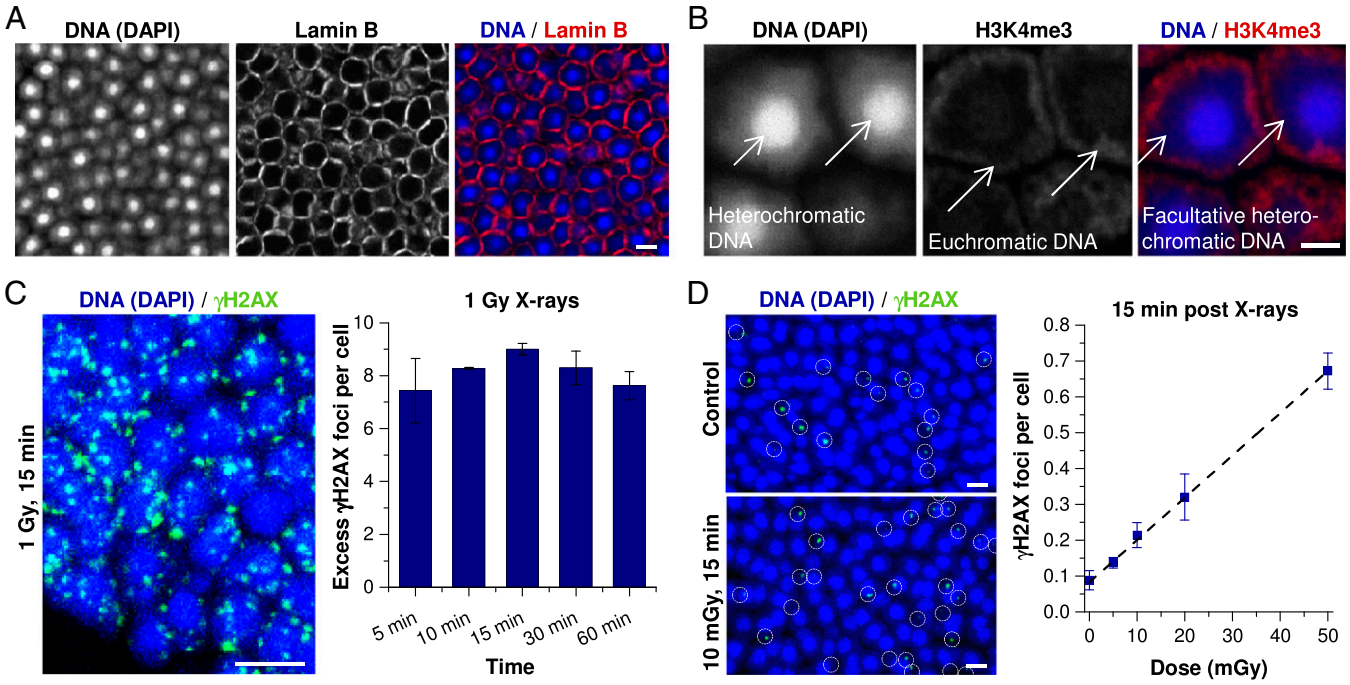

Fig. 1. γH2AX foci in mouse photoreceptors after low X-ray doses. (*A*) IF image of Lamin B in mouse photoreceptors. (Scale bar: 5 μm.) (*B*) IF image of H3K4me3 in mouse photoreceptors. Different chromatin regions in the nucleus are indicated by white arrows. (Scale bar: 2 μm.) (*C*) Time-dependent quantification of γH2AX foci per cell after receipt of 1 Gy X-irradiation. Retinae were left unirradiated or were analyzed at 5–60 min postirradiation. (*Left*) IF image (maximum intensity projection, MIP) of γH2AX in irradiated photoreceptors. (Scale bar: 5 μm.) (*Right*) Spontaneous γH2AX foci (fewer than 0.1 per cell) were subtracted. Error bars represent the SD between two retinae with 40 cells each. (*D*) Quantification and regression analysis of γH2AX foci per cell after various X-ray doses. Retinae were left unirradiated or were analyzed at 15 min after receipt of 5–50 mGy. (*Left*) IF images (MIP) of γH2AX in unirradiated or irradiated photoreceptors. γH2AX foci were framed with white circles for better visualization. (Scale bars: 5 μm.) (*Right*) Error bars representing the SD among three retinae with 1,500 cells each ($R^2 = 0.994$).

points between 5 and 60 min after delivery of 1 Gy of X-irradiation. γH2AX foci were already detected at 5 min and reached their highest value of nine foci per cell at 15 min post-IR before diminishing slightly owing to ongoing repair (Fig. 1*C*). In all subsequent experiments, we analyzed foci at 15 min post-IR. The maximum number of nine γH2AX foci per photoreceptor is substantially lower than the level of approximately 20 foci per human cell in culture (34). However, other mouse tissues, such as the brain and kidney, with cells of different nuclear architecture and size also exhibit only approximately 10.5 foci per cell, suggesting that the difference with human cells in culture is not a specific phenomenon of photoreceptors (35) (Fig. S1).

Given that radiation doses in the outer part of particle tracks are expected to be on the order of a few tens of mGy, we next characterized the dose–response of γH2AX foci formation after low radiation doses. We exposed mouse photoreceptors to 5–50 mGy of X-rays and quantified foci numbers at 15 min post-IR. We observed a linear correlation between γH2AX foci and dose with an induction rate of 11.8 ± 0.4 foci/cell/Gy (Fig. 1*D*). This result is in good agreement with the direct measurement at 1 Gy (Fig. 1*C*), and supports the view that γH2AX foci are induced linearly with dose over a large dosage range. The slight difference between the induction rates obtained at low and high doses might be explained by dosimetric errors and differences in the accuracy of foci counting at low and high doses. In summary, we have characterized the X-ray dose–response using γH2AX foci formation in mouse photoreceptors, and have shown that this tissue represents a biological system well-suited for assessing radiation doses over a substantial dosage range.

γH2AX Foci in Mouse Photoreceptors After Ion Traversals. When a single high-energy particle penetrates tissue, approximately one-half of the energy is deposited in the inner part of the track close to the particle path (within a few μm), whereas the other half is spread out by δ-electrons over a larger distance in the outer part of the track (4, 14, 36). Thus, a few cells directly hit by the ion receive a high dose, whereas numerous cells surrounding the particle path receive considerably lower doses (typically on the order of a few mGy).

To investigate the dose deposition by δ-electrons in a biological system, we exposed mouse retinae to high-energy Ti ions at very low fluences of 7.5×10^3 and 7.5×10^4 ions/cm^2. Owing to the dense packaging of photoreceptor cells, single ion traversals

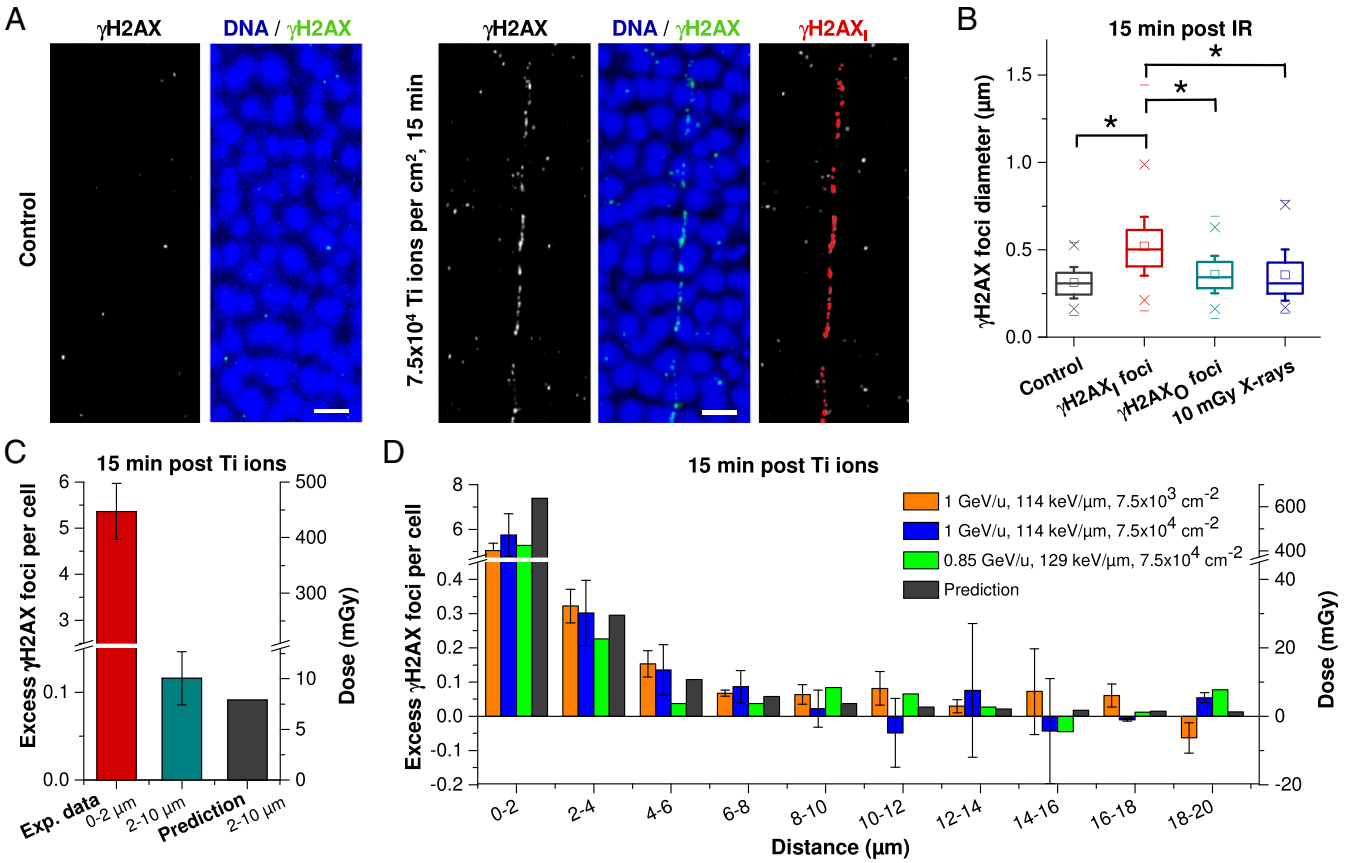

Fig. 2. γH2AX foci in mouse photoreceptors after single high LET ion traversals. (*A*) IF images (MIP) of γH2AX in unirradiated and Ti ion-irradiated mouse photoreceptors. DNA was counterstained with DAPI. (Scale bars: 5 μm.) (*Right*) γH2AX foci along the trajectory (γH2AX$_I$ foci) that were selected by eye for the calculation of the 3D regression line are marked in red. (*B*) Analysis of γH2AX foci diameters. Here 400 γH2AX$_I$ and 400 γH2AX$_O$ foci from four retinae exposed to 1 GeV/u Ti ions with 7.5×10^3 or 7.5×10^4 ions per cm^2 were analyzed and compared with 100 γH2AX foci from three retinae after 10 mGy X-rays and 100 γH2AX foci from three unirradiated retinae. The whiskers of the box (25–75% of the data points) represent the SD between the measured diameters. The ranges between the "x" below and the "x" above the boxes encompass 98% of the data. Statistical significance was tested by ANOVA; *$P < 0.05$. (*C* and *D*) Quantification of γH2AX foci per cell in different size categories. γH2AX foci and cells were enumerated in categories based on their distance to the trajectory. The number of foci per cell from images without visible ion tracks was subtracted (between 0.1 and 0.3 foci per cell, depending on particle fluence) to provide the dose contribution from a single Ti ion. Between 13 and 15 tracks with approximately 100 cells (for foci within 0–2 μm in *C*), 1,000 cells (for foci within 2–10 μm in *C*), or 2,500 cells (for foci at 0–20 μm in *D*) from one retina (for 0.85 GeV/u Ti ions) or two retinae (for 1 GeV/u Ti ions) were analyzed for each irradiation condition. Error bars represent the SD between five (*C*) or two (*D*) retinae. The predicted dose decline was calculated for 0.85 GeV/u Ti ions using the volume integral of the formula for the radial dose distribution (14) and transformed in foci per cell using the X-ray calibration curve (Fig. 1*D*).

could be readily visualized by a chain of relatively big and bright γH2AX foci over numerous cell nuclei (Fig. 2*A*; Fig. S2*A* shows the geometry of an imaged tissue section relative to the ion beam). In addition, smaller and less intense γH2AX foci were observed in the cells surrounding the particle trajectory, representing isolated DSBs induced by δ-electrons (Fig. 2*A*). The average number of ion traversals visible on a single microscopic image of approximately $100 \times 100 \times 12$ μm^3 was less than one after irradiation with 7.5×10^3 and 7.5×10^4 ions/cm^2 and increased proportionally with higher fluences (Fig. S2*B*).

To reconstruct the trajectory of the particle in the tissue, we approximated the location of each focus by its center and performed a 3D regression analysis of the chain of foci representing the inner part of the track (hereinafter termed γH2AX$_I$; indicated in red in Fig. 2*A*, *Right*, and displayed in 3D in Fig. S2*C*). We then calculated the distance of all γH2AX foci in the outer region of the track (γH2AX$_O$) to the approximated ion trajectory. Because irradiation occurred in living tissue, whereas the analysis of foci position was performed in tissue after fixation, cutting, and staining, we performed control experiments to verify that cell dimensions were not altered by this procedure (Fig. S2*D*).

The first step of our analysis involved distinguishing the γH2AX$_I$ foci in the inner part of the track from the γH2AX$_O$ foci in the surrounding area. For this analysis, we separated γH2AX foci located <2 μm from the regression line from foci located farther away. Approximately 99% of the γH2AX$_I$ foci that were identified by eye to represent the inner part were positioned within 2 μm (Fig. S2*E*). We then measured the size and intensity of each focus and confirmed our visual impression that γH2AX$_I$ foci along the trajectory were on average larger (Fig. 2*B*) and brighter (Fig. S2*F*) than γH2AX$_O$ foci in the surrounding region (diameter, ∼0.5 μm vs. ∼0.3 μm; mean signal intensity, 142 vs. 99). Interestingly, the γH2AX$_O$ foci were similar in size to X-ray–induced foci, consistent with the notion that foci after X-irradiation as well as foci in the outer part of the particle track are induced by sparsely ionizing δ-electrons.

We next determined the number of foci per cell below and above the 2 μm limit. For this, we approximated the location of each cell by its center. Thus, a cell with its center inside the 2 μm border was considered to fall within this region even though it partly protruded beyond the 2 μm limit, whereas a cell with its center outside the 2 μm border was not considered for the 0–2 μm category even if it protruded inside this area. We obtained an average of 5.4 γH2AX foci/cell inside the 2-μm border and 0.12 γH2AX foci/cell at 2–10 μm (Fig. 2*C*).

Because both γH2AX$_O$ and X-ray–induced γH2AX foci originate from secondary electrons, we converted the number of 0.12 γH2AX foci/cell into a dose of 10 mGy by using the induction rate of 11.8 foci/cell per Gy obtained in Fig. 1*D*. This dose of 10 mGy, which was evaluated based solely on biological measurements, is in excellent agreement with a theoretical track structure model that predicts an average dose of approximately 8 mGy at 2–10 μm around Ti ion trajectories (14). These results provide proof of principle that our biological dosimetry approach yields meaningful dose estimates in the low-dose range.

In the second step of our analysis, we investigated the radial decline in dose with increasing lateral distance from the particle path. We extended the analysis up to a distance of 20 μm and assessed the number of γH2AX foci per cell in 10 categories with a size of 2 μm each. We observed a decrease in γH2AX foci per cell in the first four categories up to 8 μm, which is in reasonable agreement with the theoretically predicted decline with increasing distance from the approximated trajectory (Fig. 2*D*). However, the agreement between γH2AX foci and predicted X-ray dose is less convincing in the first category (0–2 μm) where the measured foci arise from the densely ionized inner part of the particle tracks. Moreover, γH2AX foci numbers per cell varied considerably for categories larger than 8 μm, precluding a reliable analysis of the dose profile above this distance. Thus, despite the apparently good correlation between measured foci and predicted doses, this agreement was essentially limited to three size categories.

Radial and Longitudinal Distance Analysis of γH2AX Foci. To further refine the observed decline of γH2AX foci with increasing distance from the particle trajectory, we enhanced the statistical power in the categories further away from the trajectory where low γH2AX foci numbers resulted in high variations. The enhancement was achieved by defining categories that increase in width with increasing distance from the trajectory. We applied a logarithmic scale in which the distance between 0.1 and 20 μm is divided into 36 categories, with the width of each category increasing proportionally to the distance from the trajectory. This procedure reduces the data scatter in the larger categories, but has limitations for the smaller categories close to the particle trajectory (below approximately 0.5 μm), because the number of cells in these categories is very small. Thus, we introduced a further step in the analysis and reconstructed the analyzed tissue volume using small voxels with a dimension of $0.8 \times 0.8 \times 0.645$ μm^3 (Fig. S3*A*).

Using the above-described procedures, we determined the number of γH2AX foci per voxel as a function of the logarithm of the distance to the approximated particle trajectory. We also used a logarithmic scale for the vertical axis, given that a double-logarithmic plot allows visualization of the expected $1/r^2$ dependency as a linear function. For the three independent experiments from Fig. 2*D*, we obtained a plateau for γH2AX foci per voxel in the inner region up to a distance of approximately 0.4 μm, followed by a decrease slightly steeper than a $1/r^2$ dependency between 0.4 and 4 μm and by another plateau region above 4 μm (Fig. 3*A*). Although the decreasing foci numbers in the middle region roughly follow the theoretical prediction, the plateaus in the smaller and larger categories reflect expected experimental restrictions. The resolution of the focus structure with a typical size of roughly 0.5 μm and slight foci movement processes (37, 38) (Fig. S2*E*) might contribute to the deviation from the $1/r^2$ dependency below 0.4 μm, and also might give rise to a slightly steeper decrease than expected above 0.4 μm. Moreover, dose depositions from neighboring particles below or above the analyzed tissue slices represent a background dose and contribute to foci numbers in larger categories, which can explain the deviation from the $1/r^2$ dependency above 4 μm.

We next compared our experimental data with a theoretical model for high-LET radiation that is based on the dose deposition within particle tracks and takes the restrictions of the experimental system into account. We exploited the LEM (14) and considered the track structure description of the local doses deposited around a particle trajectory, as well as the enhanced DSB production for high doses (i.e., close to the trajectory) from the induction of two single-strand breaks from two different δ-electrons. We found that the latter effect played only a marginal role in the particle energies used, however, and had only a slight affect on the simulated focus yields in the inner part of the track. Fig. 3*A* shows that the simulation reflects the experimental foci distributions. In particular, the dose decrease for intermediate distances was well reproduced and slightly steeper than the expected $1/r^2$ dependency. For small distances (< ∼0.4 μm), the number of foci was slightly higher in the simulation compared with the experiments. For large distances (> ∼4 μm), the data from the three different experiments lie within the predictions for the two different ion fluences used in these experiments.

To evaluate the fluence dependency of the background dose with better statistics, we also analyzed images from irradiated retinae without visible particle tracks. Of note, the two high fluences provided a substantially higher background dose than the low fluence (Fig. S3*B*).

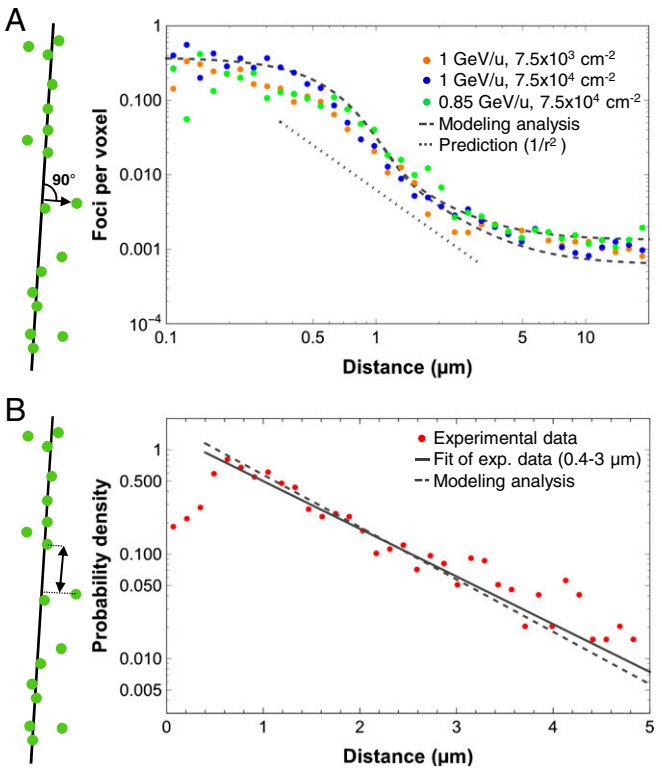

Fig. 3. Radial and longitudinal distance analysis of γH2AX foci. (*A*) Radial distance analysis of γH2AX foci perpendicular to the trajectory. The analyzed part of the tissue was reconstructed using approximately 233 voxels per cell, and the number of γH2AX foci per voxel was determined from the data presented in Fig. 2*D*. The lower and upper dashed curves represent the results of simulations based on LEM for fluences of 7.5×10^3 and 7.5×10^4 ions/cm^2, respectively. The spontaneous number of 0.00054 γH2AX foci per voxel obtained from nonirradiated retinae of the same experiments was added to the simulated curves to allow comparison with the experimental results. The dotted curve representing the theoretical $1/r^2$ dependency is down-shifted for clarity. (*B*) Longitudinal distance analysis of γH2AX foci along the trajectory. For γH2AX foci closer than 2 μm to the approximated trajectory, the longitudinal distances between next neighboring foci and the resulting probability densities of foci distances were calculated. Data for the three irradiation conditions were pooled. An exponential fit was performed to obtain the average distance between the observed foci (solid line), which is compared with results of a simulation based on LEM (for 0.85 GeV/u Ti ions; dashed line).

Along with the shape of the radial dose distribution, the LET is another characteristic parameter of the track structure, describing the amount of energy deposited along the ion track. Thus, we also determined the distance distribution of foci along the particle path, hereinafter called the longitudinal distance distribution. We considered all foci falling within a radial distance of 2 μm to the approximated ion trajectory and calculated the distance of the next neighboring foci by transforming their spatial coordinates to their position along the track. The distribution of distances decreased essentially exponentially above foci distances of 0.4 μm (i.e., along a straight line in a semilogarithmic diagram where the distance between 0 and 5 μm is divided into 35 categories of equal width), indicating that foci induction along the track is random and follows Poissonian statistics (Fig. 3*B*). This observation confirms a previous study (39) and justifies the random induction distribution of lesions along ion tracks used in almost all model approaches. Deviations from the exponential decrease below 0.4 μm might be explained by limitations in the resolution of foci structure, such that nearby DSBs are monitored as a single γH2AX focus.

DSB clustering in the inner part of the track is also supported by the difference between the simulation and the experimental data describing the radial dose distribution shown in Fig. 3*A* and by our analysis of foci sizes in Fig. 2*B* and foci intensities in Fig. S2*F*. This notion is in line with the observed saturation of foci numbers along tracks of high- and ultrahigh-LET particles (40–42). The slope of the solid curve, which reflects the average distance between observed foci, was calculated as 0.95 μm by a fit of the data between 0.4 and 3 μm. We restricted the fit to 3 μm because the presence of intercellular space might lead to a slight overrepresentation of large foci distances. Similar to the analysis of the radial dose distribution, we modeled the longitudinal distance distribution by implementing the condition that foci closer than 0.4 μm cannot be resolved owing to clustering (Fig. 3*B*). Using the track structure model of LEM, we obtained an average distance of 0.87 μm between the next neighboring foci, which is in reasonable agreement with the experimentally determined value of 0.95 μm.

Conclusions

Charged particles are generally more effective per unit dose than X-rays in inducing early and late biological effects. This increased effectiveness is exploited in cancer therapy against radioresistant tumors, but carries a higher risk for normal tissues exposed to α-particles on earth or protons and heavy ions during space travel. The ultimate reason for this high effectiveness is the spatial distribution of the induced DNA damage. For many decades, biophysical models were built on track structure models to predict increased effectiveness, yet a direct biological benchmark of these models was hitherto lacking. We applied a biological approach to assess the spatial DNA lesion and dose distribution of single charged particles. Whereas all previous studies used 2D cell culture systems, our biodosimetric study uses the mouse retina as a model tissue and uses 3D microscopic detection of DNA lesions (foci representing DSBs or more complex lesions) that arise in the nuclei of retina cells after irradiation. Calibration studies with X-rays showed that these lesions are induced linearly with dose over a large dosage range, allowing the transformation between the lesion distribution and the corresponding dose distribution. The biologically obtained distributions are in excellent agreement with results from the LEM approach that was carried out independently without any fitting parameters.

Our measurements reveal that cells hit directly by single Ti ions form a chain of foci along their particle trajectory that corresponds to an average dose in the cells of ~0.5 Gy. In contrast, neighboring cells not hit directly by primary particles but exposed to far-reaching secondary electrons (δ-electrons) show much lower dose depositions, on the order of a few mGy. Strikingly, we were able to assess the radial dose distribution of single particle tracks with submicrometer resolution and could confirm the $1/r^2$ dependency of the dose deposition by δ-electrons, which hitherto has been determined only with physical approaches in inorganic material, usually in gases. Moreover, the biological measurements indicate the presence of a background dose at larger distances from primary particles that arises as a result of additive dose contributions from several independent particles.

Along with determining the lateral dose distribution, we were able to assess the induction of foci along the track of single Ti ions. We have shown that this longitudinal energy deposition follows Poissonian statistics, indicating that the lesions are induced independently. This analysis validates the random distribution of lesions induced along ion tracks, an assumption that has been used in almost every model approach but until now has not been clearly verified with a biological model system. Collectively, our results contribute to benchmark the track structure model adopted in the LEM and in LEM-based charged particle treatment planning software. Finally, our comparison of the biological measurements and the theoretical predictions revealed a slight underrepresentation of foci induction close to the inner

part of the particle track, which is consistent with the notion that several nearby DSBs in this high-dose region can form a single, microscopically detectable focus. Such DSB clustering was previously observed by others (40, 43–46) and is also evident from our analysis of foci sizes and intensities showing that foci in the inner part of the particle track were on average larger and brighter than foci in the outer part of the track.

Cells hit directly by the track core can have a low probability of survival, but the tissue exposed in the penumbra will almost certainly survive with little damage. Because the extension of the penumbra increases with particle velocity, tissues exposed to very high-energy ions, such as those in space or used in therapy, will experience hotspots of high doses and large volumes with low dose exposure. Controversy surrounding the effects of low doses persists (2, 47, 48), but our results support the view that every exposure to charged particles should be considered a 3D entanglement of high-dose and low-dose DNA damage induction in tissues.

Materials and Methods

All animal experiments were approved by the Regional Board of Darmstadt. Details of the preparation, irradiation, and immunostaining of retina explants; image acquisition and evaluation; and modeling analysis are provided in *SI Materials and Methods*.

Preparation of Retina Explants. After the mice were killed, the eyes were removed, and the retinae together with lenses and vitreous bodies were isolated and cultured in medium before irradiation.

Irradiation. Low-LET irradiation was performed with an X-ray machine at two different settings. High-LET Ti ion irradiation was performed at a synchrotron accelerator of the GSI.

ACKNOWLEDGMENTS. Work in M.L.'s laboratory is supported by the German Aerospace Center (Grant 50WB1227), the European Space Agency (Grant AO-10-IBER-17), the Federal Ministry of Education and Research (Grant 02NUK017E), and the Deutsche Forschungsgemeinschaft (Graduate School Grant GRK1657). Work in M.D.'s biophysics group is supported by the Deutsche Forschungsgemeinschaft (Graduate School Grant GRK1657).

1. Durante M, Cucinotta FA (2008) Heavy ion carcinogenesis and human space exploration. *Nat Rev Cancer* 8(6):465–472.
2. Brenner DJ, et al. (2003) Cancer risks attributable to low doses of ionizing radiation: Assessing what we really know. *Proc Natl Acad Sci USA* 100(24):13761–13766.
3. Loeffler JS, Durante M (2013) Charged particle therapy: Optimization, challenges and future directions. *Nat Rev Clin Oncol* 10(7):411–424.
4. Chatterjee A, Schaefer HJ (1976) Microdosimetric structure of heavy ion tracks in tissue. *Radiat Environ Biophys* 13(3):215–227.
5. Kiefer J, Straaten H (1986) A model of ion track structure based on classical collision dynamics. *Phys Med Biol* 31(11):1201–1209.
6. Dingfelder M, et al. (2008) Comparisons of calculations with PARTRAC and NOREC: Transport of electrons in liquid water. *Radiat Res* 169(5):584–594.
7. Emfietzoglou D, Moscovitch M (2003) Secondary electron spectra for fast proton impact on gaseous and liquid water. *Nucl Instrum Methods Phys Res B* 209(0):239–245.
8. Friedland W, Kundrát P (2013) Track structure based modelling of chromosome aberrations after photon and alpha-particle irradiation. *Mutat Res* 756(1-2):213–223.
9. Plante I, Ponomarev AL, Cucinotta FA (2013) Calculation of the energy deposition in nanovolumes by protons and HZE particles: Geometric patterns of initial distributions of DNA repair foci. *Phys Med Biol* 58(18):6393–6405.
10. Wang H, Vassiliev ON (2014) Radial dose distributions from protons of therapeutic energies calculated with Geant4-DNA. *Phys Med Biol* 59(14):3657–3668.
11. Watanabe R, et al. (2011) Monte Carlo simulation of radial distribution of DNA strand breaks along the C and Ne ion paths. *Radiat Prot Dosimetry* 143(2-4):186–190.
12. Katz R, Zachariah R, Cucinotta FA, Zhang C (1994) Survey of cellular radiosensitivity parameters. *Radiat Res* 140(3):356–365.
13. Waligórski MP, Grzanka L, Korcyl M (2015) The principles of Katz's cellular track structure radiobiological model. *Radiat Prot Dosimetry* 166(1–4):49–55.
14. Elsässer T, Cunrath R, Krämer M, Scholz M (2008) Impact of track structure calculations on biological treatment planning in ion radiotherapy. *New J Phys* 10(7):075005.
15. Friedrich T, Scholz U, Elsässer T, Durante M, Scholz M (2012) Calculation of the biological effects of ion beams based on the microscopic spatial damage distribution pattern. *Int J Radiat Biol* 88(1-2):103–107.
16. Schipler A, Iliakis G (2013) DNA double-strand-break complexity levels and their possible contributions to the probability for error-prone processing and repair pathway choice. *Nucleic Acids Res* 41(16):7589–7605.
17. Rogakou EP, Pilch DR, Orr AH, Ivanova VS, Bonner WM (1998) DNA double-stranded breaks induce histone H2AX phosphorylation on serine 139. *J Biol Chem* 273(10):5858–5868.
18. Rothkamm K, Löbrich M (2003) Evidence for a lack of DNA double-strand break repair in human cells exposed to very low x-ray doses. *Proc Natl Acad Sci USA* 100(9):5057–5062.
19. Sedelnikova OA, Rogakou EP, Panyutin IG, Bonner WM (2002) Quantitative detection of (125)IdU-induced DNA double-strand breaks with gamma-H2AX antibody. *Radiat Res* 158(4):486–492.
20. Kinner A, Wu W, Staudt C, Iliakis G (2008) Gamma-H2AX in recognition and signaling of DNA double-strand breaks in the context of chromatin. *Nucleic Acids Res* 36(17): 5678–5694.
21. Löbrich M, et al. (2010) GammaH2AX foci analysis for monitoring DNA double-strand break repair: Strengths, limitations and optimization. *Cell Cycle* 9(4):662–669.
22. Grudzenski S, Kuefner MA, Heckmann MB, Uder M, Löbrich M (2009) Contrast medium-enhanced radiation damage caused by CT examinations. *Radiology* 253(3): 706–714.
23. Kuefner MA, et al. (2010) Effect of CT scan protocols on x-ray–induced DNA double-strand breaks in blood lymphocytes of patients undergoing coronary CT angiography. *Eur Radiol* 20(12):2917–2924.
24. Löbrich M, et al. (2005) In vivo formation and repair of DNA double-strand breaks after computed tomography examinations. *Proc Natl Acad Sci USA* 102(25):8984–8989.
25. Rothkamm K, Balroop S, Shekhdar J, Fernie P, Goh V (2007) Leukocyte DNA damage after multi-detector row CT: A quantitative biomarker of low-level radiation exposure. *Radiology* 242(1):244–251.
26. Bonner WM, et al. (2008) GammaH2AX and cancer. *Nat Rev Cancer* 8(12):957–967.
27. Redon CE, et al. (2011) γ-H2AX detection in peripheral blood lymphocytes, splenocytes, bone marrow, xenografts, and skin. *Methods Mol Biol* 682:249–270.
28. Barnard S, et al. (2015) The first gamma-H2AX biodosimetry intercomparison exercise of the developing European biodosimetry network RENEB. *Radiat Prot Dosimetry* 164(3):265–270.
29. Moquet J, Barnard S, Rothkamm K (2014) Gamma-H2AX biodosimetry for use in large-scale radiation incidents: Comparison of a rapid "96-well lyse/fix" protocol with a routine method. *PeerJ* 2:e282.
30. Kiefer J (2008) The physical basis for the biological action of heavy ions. *New J Phys* 10(7):075004.
31. Grudzenski S, Raths A, Conrad S, Rübe CE, Löbrich M (2010) Inducible response required for repair of low-dose radiation damage in human fibroblasts. *Proc Natl Acad Sci USA* 107(32):14205–14210.
32. Frohns A, Frohns F, Naumann SC, Layer PG, Löbrich M (2014) Inefficient double-strand break repair in murine rod photoreceptors with inverted heterochromatin organization. *Curr Biol* 24(10):1080–1090.
33. Solovei I, et al. (2009) Nuclear architecture of rod photoreceptor cells adapts to vision in mammalian evolution. *Cell* 137(2):356–368.
34. Kegel P, Riballo E, Kühne M, Jeggo PA, Löbrich M (2007) X-irradiation of cells on glass slides has a dose-doubling impact. *DNA Repair (Amst)* 6(11):1692–1697.
35. Rube CE, et al. (2008) DNA double-strand break repair of blood lymphocytes and normal tissues analyzed in a preclinical mouse model: Implications for radiosensitivity testing. *Clin Cancer Res* 14(20):6546–6555.
36. Cucinotta FA, Nikjoo H, Goodhead DT (1998) The effects of delta rays on the number of particle-track traversals per cell in laboratory and space exposures. *Radiat Res* 150(1):115–119.
37. Jakob B, et al. (2011) DNA double-strand breaks in heterochromatin elicit fast repair protein recruitment, histone H2AX phosphorylation and relocation to euchromatin. *Nucleic Acids Res* 39(15):6489–6499.
38. Jakob B, Splinter J, Durante M, Taucher-Scholz G (2009) Live cell microscopy analysis of radiation-induced DNA double-strand break motion. *Proc Natl Acad Sci USA* 106(9): 3172–3177.
39. Costes SV, et al. (2007) Image-based modeling reveals dynamic redistribution of DNA damage into nuclear sub-domains. *PLOS Comput Biol* 3(8):e155.
40. Jakob B, Taucher-Scholz G (2006) Interaction of heavy ions with nuclear chromatin: Spatiotemporal investigations of biological responses in a cellular environment. *Nucl Instrum Methods Phys Res B* 245(1):292–297.
41. Vadhavkar N, et al. (2014) Combinatorial DNA damage pairing model based on X-ray–induced foci predicts the dose and LET dependence of cell death in human breast cells. *Radiat Res* 182(3):273–281.
42. Neumaier T, et al. (2012) Evidence for formation of DNA repair centers and dose-response nonlinearity in human cells. *Proc Natl Acad Sci USA* 109(2):443–448.
43. Goodhead DT (1994) Initial events in the cellular effects of ionizing radiation: Clustered damage in DNA. *Int J Radiat Biol* 65(1):7–17.
44. Nakajima NI, et al. (2013) Visualisation of γH2AX foci caused by heavy ion particle traversal: Distinction between core track versus non-track damage. *PLoS One* 8(8): e70107.
45. Asaithamby A, Chen DJ (2011) Mechanism of cluster DNA damage repair in response to high-atomic number and energy particles radiation. *Mutat Res* 711(1-2):87–99.
46. Asaithamby A, Hu B, Chen DJ (2011) Unrepaired clustered DNA lesions induce chromosome breakage in human cells. *Proc Natl Acad Sci USA* 108(20):8293–8298.
47. Brenner DJ, Hall EJ (2012) Cancer risks from CT scans: Now we have data, what next? *Radiology* 265(2):330–331.
48. Mullenders L, Atkinson M, Paretzke H, Sabatier L, Bouffler S (2009) Assessing cancer risks of low-dose radiation. *Nat Rev Cancer* 9(8):596–604.